Josephson Diode Effect in High-Mobility InSb Nanoflags

Bianca Turini, Sedighe Salimian, Matteo Carrega, Andrea Iorio, Elia Strambini, Francesco Giazotto, Valentina Zannier, Lucia Sorba, and Stefan Heun*

ACCESS	Metrics & More	Article Recommendations	Supporting Information

ABSTRACT: We report nonreciprocal dissipation-less transport in single ballistic InSb nanoflag Josephson junctions. Applying an in-plane magnetic field, we observe an inequality in supercurrent for the two opposite current propagation directions. Thus, these devices can work as Josephson diodes, with dissipation-less current flowing in only one direction. For small fields, the supercurrent asymmetry increases linearly with external field, and then it saturates as the Zeeman energy becomes relevant, before it finally decreases to zero at higher fields. The effect is maximum when the in-plane field is perpendicular to the current vector, which identifies Rashba spin–orbit coupling as the main symmetry-breaking mechanism. While a variation in carrier concentration in these high-quality InSb nanoflags does not significantly influence the supercurrent asymmetry, it is instead strongly suppressed by an increase in temperature. Our experimental findings are consistent with a model for ballistic short junctions and show that the diode effect is intrinsic to this material.

KEYWORDS: *Josephson junctions, Supercurrent Diode Effect, Spin–orbit coupling, InSb, Nb*
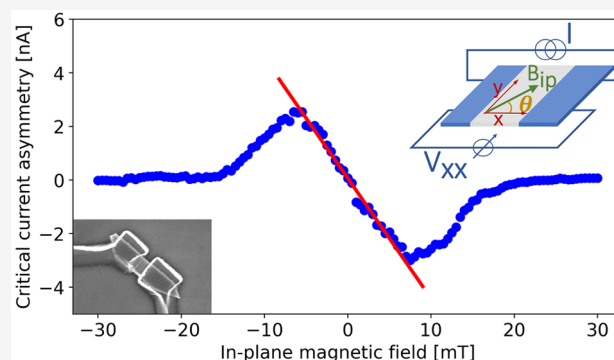
Nonreciprocal charge transport is at the heart of conventional electronics, in which a fundamental building block, the diode, is based on the p–n junction. In such systems, rectification takes place due to the presence of a heterojunction that explicitly breaks inversion symmetry. Only very recently it has been proposed that the superconducting analogue of nonreciprocal transport can be made,[1] based on similar symmetry arguments: in this case, nonreciprocity is expected when time-reversal and inversion symmetries are simultaneously broken.[2–6] Supercurrent rectification has been achieved in superconducting quantum interference devices (SQUIDs), where the flux tunability allows high rectification coefficients to be reached. However, this rectification is of extrinsic nature, being induced by asymmetric junctions and the presence of an external flux threading the SQUID.[7–10]

In fact, an intrinsic supercurrent analogue exists—the supercurrent diode effect (SDE)—whose exploitation would constitute a breakthrough for low-temperature technology and superconducting electronics. The first experimental report on the SDE, based on electrically polar materials,[11] has appeared very recently, demonstrating supercurrent rectification. Soon after, other systems[12–23] have been inspected looking at supercurrent nonreciprocal transport, complemented by theoretical efforts,[9,24–32] to shed light on the microscopic mechanisms responsible for the SDE. However, both from an experimental and a theoretical point of view, this field is still in its infancy.

During the past decade, there has been a widespread interest in the physics of hybrid systems comprising superconductors and low-dimensional semiconductors featuring strong spin–orbit coupling (SOC). Indeed, these systems offer an ideal platform to develop new architectures able to coherently control electron spin with significant impact in spintronics and topological quantum computing.[15,33–35]

Exploiting the large SOC of InAs, the authors of ref 13 have observed SDE in an array of Josephson junction (JJ) devices. Supercurrent rectification in hybrid JJs has been also referred to as the Josephson diode effect (JDE). Here, the combination of SOC and superconducting proximity leads to a strong interaction between spin, charge, and superconducting phase, which is the working principle of the φ_0 junction. In such devices, the current–phase relation (CPR) is shifted by an anomalous phase φ_0.[36] Moreover, φ_0 junctions can be considered the precursors of the Josephson diode: as discussed in ref 13, highly transmissive junctions, which operate in the short-junction regime, are characterized by a skewed CPR,
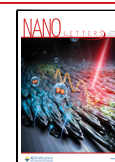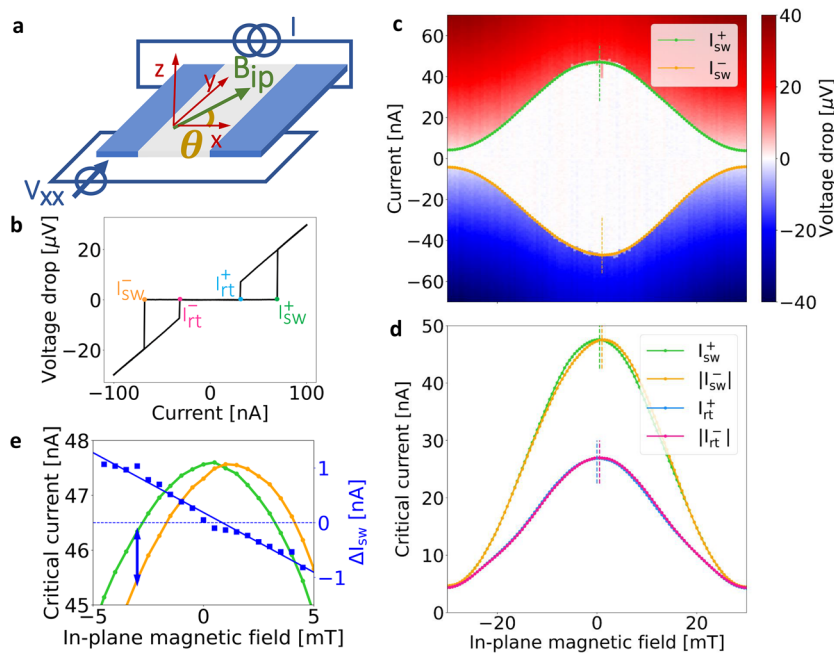
Figure 1. Switching current dependence on in-plane magnetic field. (a) Sketch of the measurement schematics. Also the angle θ between the orientation of the in-plane magnetic field B_{ip} and the direction of current flow I is indicated. (b) $V-I$ characteristics at T = 30 mK, B = 0. The difference between switching and retrapping current, defined in the plot, is clearly visible. (c) Voltage drop across the junction versus applied current bias I and in-plane magnetic field B_{ip}. The green (orange) dots indicate the positive (negative) switching currents, as defined in the main text. (d) The switching current demonstrates a clear asymmetry between the positive and negative branches, shown in green and orange, respectively. The blue and pink lines correspond to the positive and negative retrapping current. In both cases, the maximum of the curves is different: the negative branch is higher for positive values of the magnetic field, and the relation is reversed for negative field. (e) The differences in switching current are better seen in a zoom-in of panel d to the region around $B_{ip} \sim 0$. The panel also shows that $\Delta I_{sw} = I_{sw}^+ - |I_{sw}^-|$ changes linearly with in-plane magnetic field around B_{ip} = 0. The blue arrow visualizes the definition of ΔI_{sw}. There is a small global field offset (0.75 mT) that we attribute to a residual magnetization of the cryostat. Device G5, angle θ = 129°, T = 30 mK, and V_{bg} = 40 V.

which leads to supercurrent rectification in the presence of an anomalous phase shift.

In this context, InSb represents a valid platform. InSb has a narrow band gap (0.23 eV),[33,37,38] and a small effective mass (m^* = 0.018 m_e),[33,39−44] and exhibits a strong SOC and a large Landé g-factor (|g^*| ∼ 50).[45] In InSb 2D nanostructures, a similar value is measured in the out-of-plane direction, while the in-plane value g_{ip}^* is reduced by a factor of 2, independently of the crystallographic direction ($g_x^* \sim g_y^* \sim 25$).[33,41,44] Moreover, a Rashba spin−orbit strength of $\alpha_R \sim 0.42$ eV Å was reported for InSb nanosheets,[34] which yields a spin−orbit energy $E_{so} = (m^* \alpha_R^2)/(2\hbar^2) \sim 200$ μeV.

In this work, we present the first report of JDE in single planar JJs based on high-quality InSb nanoflags. These structures[46,47] have been used to form ballistic planar JJs, upon deposition of superconducting contacts.[43,48] Owing to their intrinsic strong SOC and sizable superconducting proximity,[41,46,47,49,50] they become a natural platform to investigate JDE and obtain insight on its microscopic mechanism.

Previous experiments on analogous devices show a Nb-induced gap of Δ^* = 160 μeV.[48] This value is close to E_{so}, suggesting that SOC plays a relevant role in the physics of these InSb JJs. The high quality of the material is a crucial feature that permits it to work in the ballistic regime, allowing for the direct observation of a nonreciprocal supercurrent. In addition, the dependence of the JDE on external parameters can provide valuable information on the symmetry-breaking

mechanisms at play. Our observations are consistent with a dominant Rashba coupling related to structural inversion asymmetry. We provide a direct demonstration of JDE in a single and scalable planar JJ, which constitutes a crucial step forward in the understanding of the JDE mechanism.

The system under investigation is a superconducting−normal metal−superconducting (SNS) planar JJ, where the N region consists of an InSb quasi-2D nanostructure. The two devices discussed in this publication (G4 and G5) are operating in the short ballistic regime. Details on device fabrication and characteristics are provided in the Supporting Information (SI). Figure 1b shows a characteristic $V-I$ curve of device G4. We can clearly distinguish the switching (I_{sw}) and the retrapping (I_{rt}) currents.

We report evidence of the JDE in these devices, showing that it only requires an in-plane magnetic field orthogonal to the direction of current flow. Figure 1c shows the voltage drop across junction G5 versus applied current bias I and in-plane magnetic field B_{ip}, with the relative angle set to θ = 129° (cf., Figure 1a). The data was taken by increasing the bias from zero to positive (negative) values, to exclude a current heating of the device before the switching event. The superconducting region, defined by dissipation-less charge transport, corresponds to the white area. The supercurrent is maximum around zero in-plane magnetic field and decreases with increasing field until B_{ip} = ± 30 mT, for which it is nearly but not completely suppressed.

From the map, positive and negative switching currents can be extracted. The values of positive switching current I_{sw}^+ and negative switching current I_{sw}^- are included in Figure 1c as
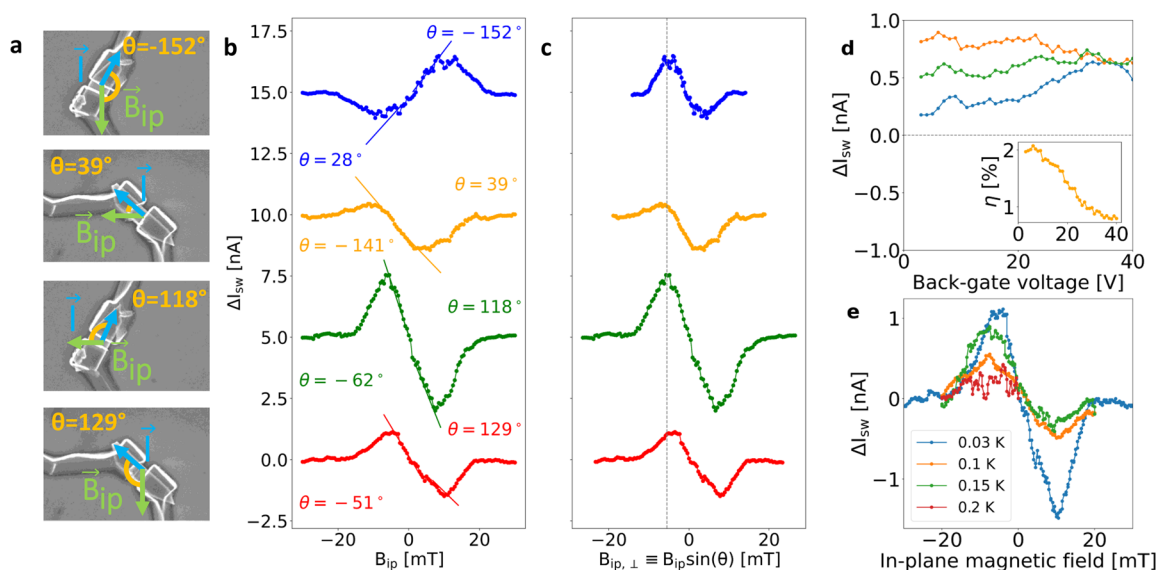
Figure 2. Behavior of the JDE with in-plane magnetic field, perpendicular component of the in-plane field, back-gate voltage, and temperature. (a) SEM images indicating the relative angle between B_{ip} and I (for positive field) for the measurements shown in panels b and c. For negative field, the angle is offset by 180°. (b) Asymmetry versus in-plane field for different orientations of the devices. Here, the blue and green curves correspond to device G4, while the yellow and red curves correspond to G5. Linear fits for small values of the field are also shown (negative and positive branch fitted independently). (c) Asymmetry versus the component of the magnetic field perpendicular to the current flow. The maximum of ΔI_{sw} is observed for $B_{ip,\perp} = -6 \pm 1$ mT for each curve (indicated by the dashed line). The amplitude of the effect is maximum when θ is close to $\pm 90°$, i.e., when the in−plane magnetic field is perpendicular to the current vector, as explained in the main text. Note that the polarity of the curve at $\theta = -152°$ in panel c is reversed with respect to panel b due to the sign of $\sin(\theta)$. In panels b and c, the curves are offset by 5 nA each for clarity. (d) Asymmetry versus back-gate voltage, for three different values of the applied in-plane magnetic field: blue, $B_{ip} = -6$ mT; orange, $B_{ip} = -8$ mT; green, $B_{ip} = -10$ mT. The inset shows the diode rectification coefficient η as a function of back-gate voltage, for $B_{ip} = -8$ mT. (e) Temperature dependence of the asymmetry. For panels d and e, Device G5.

green and orange dots, respectively. Careful analysis shows that the pattern is slightly skewed with opposite polarity for the two sweep directions. The position of the maximum (minimum) value of I_{sw}^+ (I_{sw}^-) is indicated in the panel by dashed lines. Note that the two sweep directions are measured consequentially for each value of B_{ip}; hence, a simple residual magnetization could not explain the opposite skewness of the two patterns. Interestingly, the maximum of the switching current is not observed for zero magnetic field, as one would expect for a standard Fraunhofer-like pattern, but is slightly shifted to a finite magnetic field whose sign depends on the sweeping direction. Therefore, we observe that the magnitude of the positive (negative) switching current *increases* with respect to the value at zero field for small negative (positive) values of the magnetic field.

The asymmetry between the positive and negative branches is more clearly visible by comparing the absolute values of the two curves, shown in Figure 1d,e. For negative magnetic field, $I_{sw}^+ \geq |I_{sw}^-|$, while for positive field, $I_{sw}^+ \leq |I_{sw}^-|$. Thus, for nonzero values of B_{ip}, there exists a range of bias current values for which the transport across the junction is nondissipative only in one direction, indicating the presence of JDE. In addition, the action of the Josephson rectifier is reversed with the sign of the magnetic field. In the same measurement, also the retrapping current was recorded when sweeping the current back to zero after each switching event. These data are shown in Figure 1d, as well. The same JDE is observed, albeit with smaller magnitude. Qualitatively identical results were also observed for device G4, as reported in the SI.

We use the difference in the switching currents $\Delta I_{sw} = I_{sw}^+ - |I_{sw}^-|$ to quantify the JDE. The dependence of

ΔI_{sw} on magnetic field is presented in Figure 2b. To consider the asymmetry beyond the fluctuations due to stochastic switching, we performed a gentle smoothing procedure, as described in the SI. The experiment was repeated for different relative orientations of the magnetic field, as sketched in Figure 2a, to collect information about the angular dependence of the JDE. All measurements in Figure 2b show antisymmetric curves, i.e., $\Delta I_{sw}(B_{ip}) = -\Delta I_{sw}(-B_{ip})$. Furthermore, the curve for $\theta = -152°$ is flipped with respect to the others. This is consistent with the different orientations of the devices with respect to the field direction; i.e., the polarity of the ΔI_{sw} curves reflects the sign of the angle θ, which suggests that $\Delta I_{sw} \propto \vec{B}_{ip} \times \vec{I}$. We observe that ΔI_{sw} varies smoothly from a linear regime around zero field via a smooth rounded maximum at intermediate-field values to the high-field region, in which the effect is completely suppressed. The general trend is consistent with previous experiments, in which however a more rapid quenching was observed.[13] To highlight the linear regime around zero field, we have added linear best fits at the origin of each curve (negative and positive branch fitted independently). A similar and consistent behavior was also observed for the retrapping current, as shown in the SI.

To disentangle the contributions of the parallel $(B_{ip,\parallel})$ and perpendicular $(B_{ip,\perp})$ components of the field, computed with respect to the direction of current flow, we mapped in Figure 2c the measured data on the effective $B_{ip,\perp}$. Note that, in the case of $\theta < 0$, the change in polarity is due to the sign of $\sin(\theta)$. In all data sets, the maximum asymmetry is observed for $B_{ip,\perp} = -6 \pm 1$ mT, while its magnitude depends on the specific orientation. Thus, the main contribution to the effect is given

by the perpendicular component of the field, consistent with $\Delta I_{sw} \propto \vec{B}_{ip} \times \vec{I}$.

Next, we study the dependence of the JDE on back-gate voltage. By setting the value of the field near the maximal ΔI_{sw} value of Device G5, we performed back-gate sweeps to the pinch-off of the devices. As shown in Figure 2d, the asymmetry is nearly constant in the explored range, which implies that the applied electrical field is not strong enough to significantly modulate spin−orbit coupling, consistently with results in similar systems.[13] On the other hand, the back gate modulates the carrier concentration very efficiently in these devices,[47] resulting in a reduction of the switching current from ∼50 nA to pinch-off in the same range,[48] see also the SI. Thus, ΔI_{sw} appears to be robust against variations in carrier concentration and therefore seems to be governed by a mechanism other than I_{sw} itself. On the other hand, the relative strength of ΔI_{sw}, or the diode rectification coefficient $\eta = \Delta I_{sw}/(I_{sw}^{+} + |I_{sw}^{-}|)$, which is the proper figure of merit to quantify the rectification effect, *increases* with decreasing gate voltage, as shown in the inset to Figure 2d.

Finally, in Figure 2e we show the influence of temperature. The amplitude of the asymmetry is rapidly reduced with increasing temperature and strongly suppressed already for $T = 200$ mK. We note that the acquisition at $T = 150$ mK is less antisymmetric, which we attribute to stochastic noise. Remarkably, while the diode effect disappears, the switching current at $T = 200$ mK is only reduced by about 20% with respect to its value at base temperature. On the other hand, the magnetic field value at which the maximum value of ΔI_{sw} is observed does not depend on temperature.

The same measurement as in Figure 1c is repeated in an out-of-plane magnetic field (no in-plane component), as shown in the inset to Figure 3a. In this case, no asymmetry is observed, consistent with previous results for similar systems.[43,48,51,52] Finally, we add that all measurements performed at $B = 0$ resulted in asymmetry values equal to zero within the noise level.

In ref 53, it has been shown that *either* the presence of an in-plane field parallel to the current direction and a Dresselhaus SOC, *or* an in-plane field perpendicular to the charge flow and a Rashba SOC is a sufficient condition for this effect to emerge. Thus, the determination of which parameter drives the JDE provides valuable information about the key acting mechanisms in the junction. Here, we have measured the JDE for different angles θ, i.e., for different relative strength of the two in-plane components. We have shown in Figure 2c that the magnitude of the effect increases with the sine of the relative angle, i.e., with the perpendicular component of the in-plane field. Since the effect of this component is mediated by the Rashba coefficient, we can state that here a key role is played by the Rashba SO interaction. On the other hand, as shown in the SI, we have observed no clear trend with the parallel component, indicating that the Dresselhaus term is of little relevance in this system, consistent with previous results reported for InAs-based JJs.[15]

Our experimental evidence presented in Figure 2c shows that the behavior of ΔI_{sw} is antisymmetric with respect to $B_{ip,\perp}$, and its maximum value is reached for $B_{ip,\perp} = -6$ mT, independent of back-gate voltage, temperature, or the relative angle θ. On the other hand, the magnitude of the effect does depend on the relative angle. The analysis in Figure 2b shows that the asymmetry depends linearly on the in-plane magnetic
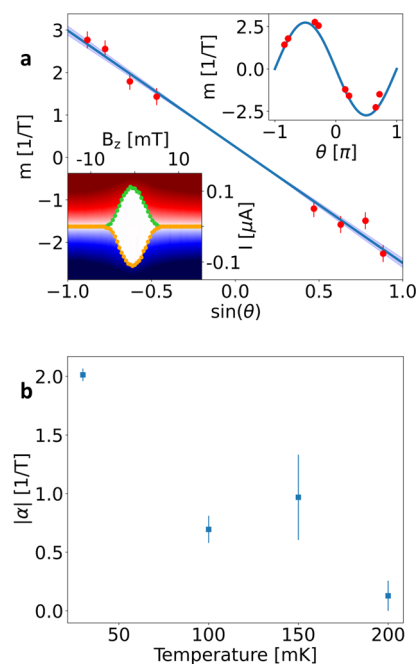
Figure 3. (a) Proportionality factor m (between rectification coefficient η and in-plane magnetic field B_{ip}, i.e., $m = \eta/B_{ip}$, see main text), plotted versus the sine of the angle θ between B_{ip} and the current flow direction. The blue line represents the best linear fit to the data, from which the value of α is extracted. The shaded region indicates the confidence interval. Upper inset: The same data plotted versus θ. The blue curve is a sine function, showing that the data points nicely follow a $\sin(\theta)$ behavior. Lower inset: Measurement of the switching current with respect to a magnetic field perpendicular to the junction plane in a similar device, with the same material and geometric parameters of G4 and G5. The figure shows the voltage drop across the junction versus applied current bias I and out-of-plane magnetic field B_z. The green (orange) dots indicate the positive (negative) switching currents, as defined in the main text. The width of the interference pattern is 4 times smaller than what we have obtained with an in-plane field. No asymmetry is observed in this configuration. (b) Proportionality factor $|\alpha|$ plotted versus T, for $\theta = 129°$ (Device G5).

field near $B_{ip} = 0$, consistent with previous experimental results[11] and theoretical predictions.[29]

To investigate the physics of this system, we consider models for the JDE in short ballistic junctions.[54,55] These models are based on the idea of finite momentum Cooper pairs via the Zeeman effect on spin−helical electrons,[29,42,56] akin to a so-called Doppler shift. In the InSb, the magnetic field introduces a Zeeman splitting term and, due to the strong SOC of the material, determines a spatially varying order parameter in the junction.[56] Consequently, the Cooper pairs acquire a finite momentum q in the direction perpendicular to the magnetic field and the SO vector. This breaks the equivalence between the two propagation directions I^{+} and I^{-} of the current. We remark that here the spatial modulation occurs in the normal region of the junction and not in the superconducting leads.

If E_{so} is much larger than the Zeeman energy $E_z = g_{ip}^{*} \mu_B B_{ip} \ll E_{so}$, energy bands of opposite spin are split, and a finite Cooper pair momentum is expected.[56] This condition is fulfilled here, since $E_z = 15 \mu$eV at 10 mT and thus much smaller than $E_{so} = 200 \mu$eV. Then, $q v_F = E_z$, with v_F the Fermi velocity, and thus $q \propto B$.[54,56] The difference between the magnitudes of the critical

currents in opposite directions $\Delta I_c = I_c^+ - |I_c^-|$ can then be calculated for small B, zero temperature, and one conductive channel as[54,55]

$$\Delta I_c = \frac{4eE_z}{\pi\hbar} + O(B^2) \quad (1)$$

Up to first order in the magnetic field, we also obtain

$$I_c^+ + |I_c^-| = \frac{2e\Delta^*}{\hbar} + O(B^2) \quad (2)$$

with e being the electron charge. This finally allows the estimation of the diode rectification coefficient η in the linear-in-field regime:

$$\eta = \frac{\Delta I_c}{I_c^+ + |I_c^-|} = \frac{2g^*\mu_B}{\pi\Delta^*}B \equiv \alpha B \quad (3)$$

Using the parameters for InSb ($g_{ip}^* = 25$ and $\Delta^* = 108\ \mu$eV, see the SI), we obtain $\alpha = 8.5$ T^{-1} or equivalently a characteristic field $B_0 = 1/\alpha = 118$ mT.

To compare this result with the experiment, for each curve shown in Figure 2b, we extract the slope m of the linear fit of ΔI_{sw} near $B_{ip} = 0$ (negative and positive branches fitted independently). In Figure 3a, the values of m are plotted versus the sine of the relative angle θ, normalized to the sum of the two switching currents at zero field (red dots). The blue line is the result of a linear fit, from which the linear coefficient $\alpha = -2.9 \pm 0.2$ T^{-1} is extracted (corresponding to $B_0 = 345$ mT), while the value of the intercept is negligible ($\beta = 0.03$ T^{-1}). The relation $m \propto \sin(\theta)$ indicates that the rectification effect increases with the perpendicular component of the in-plane field $B_{ip,\perp} = B_{ip} \sin(\theta)$.

By considering the behavior of ΔI_c at a finite field,[54,55] we obtain that the maximum is reached for $g^*\mu_B B = \sqrt{16/(\pi^2 + 16)}\ \Delta^* \approx 0.78\Delta^*$ (see the SI). Here it would thus be expected to be at $B = 58$ mT, which is higher than experimentally observed. We attribute the discrepancy to the presence of the parallel component of B_{ip}, which is expected to suppress the supercurrent flow at higher fields. Moreover, the model does not consider other effects due to the finite size of the junctions, which could be relevant in our system, as well.

The temperature dependence of the asymmetry curves, shown in Figure 2e, deserves attention. In fact, whereas the switching current hardly varies in the temperature range 30−200 mK, the JDE undergoes a nearly complete suppression. Correspondingly, the rectification coefficient $|\alpha|$ is strongly reduced with increasing temperature (see Figure 3b). The differing behavior between these two quantities originates from the fact that the JDE is strongly dependent on the presence of higher harmonics in the CPR of ballistic SNS junctions.[13] Indeed, in the case of a purely sinusoidal dependence, the anomalous phase shift does not induce any difference between I_{sw}^+ and I_{sw}^-, which correspond to the maximum and minimum of the CPR, respectively. Higher harmonics decay faster with increasing temperature, so that in the high-temperature limit, the only relevant harmonic is the lowest one; i.e, the CPR is a simple sine function. Thus, the JDE is strongly suppressed in temperature, due to the much stronger dependence of the higher harmonics with respect to the fundamental one.

In conclusion, we have demonstrated that a single planar JJ made from an InSb nanoflag can be driven into the nonreciprocal transport regime by an in-plane magnetic field applied perpendicularly to the direction of the current flow. Moreover, the extent of the rectification depends on the specific combination of the two in-plane field components. Based on symmetry arguments, we have determined that a key role is played by the Rashba SOC. Furthermore, we have elucidated the dependence of the effect on other parameters and, specifically, that increasing temperature drastically quenches supercurrent rectification. This is consistent with the absence of higher harmonics in the CPR expected at elevated temperature.

Thus, high-quality InSb nanoflags are optimal candidates to realize low-dissipation supercurrent rectifiers and to explore the physics of nonreciprocal superconductivity. Further progress in this field will be promoted by the development of microscopic theories which link the rectification quantitatively to the spin−orbit coupling strength. Then, we expect the SDE to become a useful addition to the toolbox of hybrid superconducting electronics.

■ ASSOCIATED CONTENT

■ AUTHOR INFORMATION

Corresponding Author

Stefan Heun − NEST, Istituto Nanoscienze-CNR and Scuola Normale Superiore, 56127 Pisa, Italy; ⊙ orcid.org/0000-0003-1989-5679; Email: stefan.heun@nano.cnr.it

Authors

Bianca Turini − NEST, Istituto Nanoscienze-CNR and Scuola Normale Superiore, 56127 Pisa, Italy

Sedighe Salimian − NEST, Istituto Nanoscienze-CNR and Scuola Normale Superiore, 56127 Pisa, Italy

Matteo Carrega − CNR-SPIN, 16146 Genova, Italy

Andrea Iorio − NEST, Istituto Nanoscienze-CNR and Scuola Normale Superiore, 56127 Pisa, Italy

Elia Strambini − NEST, Istituto Nanoscienze-CNR and Scuola Normale Superiore, 56127 Pisa, Italy; ⊙ orcid.org/0000-0003-1135-2004

Francesco Giazotto − NEST, Istituto Nanoscienze-CNR and Scuola Normale Superiore, 56127 Pisa, Italy

Valentina Zannier − NEST, Istituto Nanoscienze-CNR and Scuola Normale Superiore, 56127 Pisa, Italy; ⊙ orcid.org/0000-0002-9709-5207

Lucia Sorba − NEST, Istituto Nanoscienze-CNR and Scuola Normale Superiore, 56127 Pisa, Italy

Complete contact information is available at:
https://pubs.acs.org/10.1021/acs.nanolett.2c02899

Notes

The authors declare no competing financial interest.

■ ACKNOWLEDGMENTS

■ REFERENCES

(1) Hu, J.; Wu, C.; Dai, X. Proposed Design of a Josephson Diode. *Phys. Rev. Lett.* **2007**, *99*, 067004.

(2) Wakatsuki, R.; Saito, Y.; Hoshino, S.; Itahashi, Y. M.; Ideue, T.; Ezawa, M.; Iwasa, Y.; Nagaosa, N. Nonreciprocal charge transport in noncentrosymmetric superconductors. *Science Advances* **2017**, *3*, No. e1602390.

(3) Qin, F.; Shi, W.; Ideue, T.; Yoshida, M.; Zak, A.; Tenne, R.; Kikitsu, T.; Inoue, D.; Hashizume, D.; Iwasa, Y. Superconductivity in a chiral nanotube. *Nat. Commun.* **2017**, *8*, 14465.

(4) Tokura, Y.; Nagaosa, N. Nonreciprocal responses from noncentrosymmetric quantum materials. *Nat. Commun.* **2018**, *9*, 3740.

(5) Hoshino, S.; Wakatsuki, R.; Hamamoto, K.; Nagaosa, N. Nonreciprocal charge transport in two-dimensional noncentrosymmetric superconductors. *Phys. Rev. B* **2018**, *98*, 054510.

(6) Yasuda, K.; Yasuda, H.; Liang, T.; Yoshimi, R.; Tsukazaki, A.; Takahashi, K. S.; Nagaosa, N.; Kawasaki, M.; Tokura, Y. Nonreciprocal charge transport at topological insulator/superconductor interface. *Nat. Commun.* **2019**, *10*, 2734.

(7) Barone, A.; Paternò, G.*Physics and Applications of the Josephson Effect*; John Wiley & Sons, Inc., 1982.

(8) Paolucci, F.; Vischi, F.; De Simoni, G.; Guarcello, C.; Solinas, P.; Giazotto, F. Field-Effect Controllable Metallic Josephson Interferometer. *Nano Lett.* **2019**, *19*, 6263−6269.

(9) Souto, R. S.; Leijnse, M.; Schrade, C.The Josephson Diode Effect in Supercurrent Interferometers. arXiv:2205.04469 [cond-mat.mes-hall], 2022; https://arxiv.org/abs/2205.04469, submission date: 9 May 2022 (accessed 2022-08-30).

(10) Sundaresh, A.; Vayrynen, J. I.; Lyanda-Geller, Y.; Rokhinson, L. P.Supercurrent Non-reciprocity and Vortex Formation in Superconductor Heterostructures. arXiv:2207.03633 [cond-mat.supr-con], 2022; https://arxiv.org/abs/2207.03633, submission date: 8 Jul 2022 (accessed 2022-08-30).

(11) Ando, F.; Miyasaka, Y.; Li, T.; Ishizuka, J.; Arakawa, T.; Shiota, Y.; Moriyama, T.; Yanase, Y.; Ono, T. Observation of superconducting diode effect. *Nature* **2020**, *584*, 373−376.

(12) Miyasaka, Y.; Kawarazaki, R.; Narita, H.; Ando, F.; Ikeda, Y.; Hisatomi, R.; Daido, A.; Shiota, Y.; Moriyama, T.; Yanase, Y.; Ono, T. Observation of nonreciprocal superconducting critical field. *Applied Physics Express* **2021**, *14*, 073003.

(13) Baumgartner, C.; Fuchs, L.; Costa, A.; Reinhardt, S.; Gronin, S.; Gardner, G. C.; Lindemann, T.; Manfra, M. J.; Faria Junior, P. E.; Kochan, D.; Fabian, J.; Paradiso, N.; Strunk, C. Supercurrent rectification and magnetochiral effects in symmetric Josephson junctions. *Nat. Nanotechnol.* **2022**, *17*, 39−44.

(14) Wu, H.; Wang, Y.; Xu, Y.; Sivakumar, P. K.; Pasco, C.; Filippozzi, U.; Parkin, S. S. P.; Zeng, Y.-J.; McQueen, T.; Ali, M. N. The field-free Josephson diode in a van der Waals heterostructure. *Nature* **2022**, *604*, 653−656.

(15) Baumgartner, C.; Fuchs, L.; Costa, A.; Picó-Cortés, J.; Reinhardt, S.; Gronin, S.; Gardner, G. C.; Lindemann, T.; Manfra, M. J.; Junior, P. E. F.; Kochan, D.; Fabian, J.; Paradiso, N.; Strunk, C. Effect of Rashba and Dresselhaus spin−orbit coupling on supercurrent rectification and magnetochiral anisotropy of ballistic Josephson junctions. *J. Phys.: Condens. Matter* **2022**, *34*, 154005.

(16) Strambini, E.; Spies, M.; Ligato, N.; Ilić, S.; Rouco, M.; González-Orellana, C.; Ilyn, M.; Rogero, C.; Bergeret, F. S.; Moodera, J. S.; Virtanen, P.; Heikkilä, T. T.; Giazotto, F. Superconducting spintronic tunnel diode. *Nat. Commun.* **2022**, *13*, 2431.

(17) Diez-Merida, J.; Diez-Carlon, A.; Yang, S. Y.; Xie, Y. M.; Gao, X. J.; Watanabe, K.; Taniguchi, T.; Lu, X.; Law, K. T.; Efetov, D. K.Magnetic Josephson Junctions and Superconducting Diodes in Magic Angle Twisted Bilayer Graphene. arXiv:2110.01067 [cond-mat.supr-con], 2021; https://arxiv.org/abs/2110.01067, submission date: 3 Oct 2021 (accessed 2022-08-30).

(18) Bauriedl, L.; Bäuml, C.; Fuchs, L.; Baumgartner, C.; Paulik, N.; Bauer, J. M.; Lin, K.-Q.; Lupton, J. M.; Taniguchi, T.; Watanabe, K.; Strunk, C.; Paradiso, N. Supercurrent diode effect and magnetochiral anisotropy in few-layer NbSe$_2$. *Nat. Commun.* **2022**, *13*, 4266.

(19) Shin, J.; Son, S.; Yun, J.; Park, G.; Zhang, K.; Shin, Y. J.; Park, J.-G.; Kim, D.Magnetic Proximity-Induced Superconducting Diode Effect and Infinite Magnetoresistance in van der Waals Heterostructure. arXiv:2111.05627 [cond-mat.supr-con], 2021; https://arxiv.org/abs/2111.05627, submission date: 10 Nov 2021 (accessed 2022-08-30).

(20) Lin, J.-X.; Siriviboon, P.; Scammell, H. D.; Liu, S.; Rhodes, D.; Watanabe, K.; Taniguchi, T.; Hone, J.; Scheurer, M. S.; Li, J. I. A. Zero-Field Superconducting Diode Effect in Small-Twist-Angle Trilayer Graphene. *Nat. Phys.* **2022**, *18*, 1221−1227, DOI: 10.1038/s41567-022-01700-1.

(21) Pal, B.; Chakraborty, A.; Sivakumar, P. K.; Davydova, M.; Gopi, A. K.; Pandeya, A. K.; Krieger, J. A.; Zhang, Y.; Date, M.; Ju, S.; Yuan, N.; Schröter, N. B. M.; Fu, L.; Parkin, S. S. P. Josephson Diode Effect from Cooper Pair Momentum in a Topological Semimetal. *Nat. Phys.* **2022**, *18*, 1228−1233, DOI: 10.1038/s41567-022-01699-5.

(22) Hou, Y.; Nichele, F.; Chi, H.; Lodesani, A.; Wu, Y.; Ritter, M. F.; Haxell, D. Z.; Davydova, M.; Ilić, S.; Bergeret, F. S.; Kamra, A.; Fu, L.; Lee, P. A.; Moodera, J. S.Ubiquitous Superconducting Diode Effect in Superconductor Thin Films. arXiv:2205.09276 [cond-mat.supr-con], 2022; https://arxiv.org/abs/2205.09276, submission date: 20 May 2022 (accessed 2022-08-30).

(23) Gupta, M.; Graziano, G. V.; Pendharkar, M.; Dong, J. T.; Dempsey, C. P.; Palmstrøm, C.; Pribiag, V. S.Superconducting Diode Effect in a Three-Terminal Josephson Device. arXiv:2206.08471 [cond-mat.mes-hall], 2022; https://arxiv.org/abs/2206.08471, submission date: 10 Aug 2022 (accessed 2022-08-30).

(24) Kopasov, A. A.; Kutlin, A. G.; Mel'nikov, A. S. Geometry controlled superconducting diode and anomalous Josephson effect triggered by the topological phase transition in curved proximitized nanowires. *Phys. Rev. B* **2021**, *103*, 144520.

(25) Misaki, K.; Nagaosa, N. Theory of the nonreciprocal Josephson effect. *Phys. Rev. B* **2021**, *103*, 245302.

(26) Daido, A.; Ikeda, Y.; Yanase, Y. Intrinsic Superconducting Diode Effect. *Phys. Rev. Lett.* **2022**, *128*, 037001.

(27) Halterman, K.; Alidoust, M.; Smith, R.; Starr, S. Supercurrent diode effect, spin torques, and robust zero-energy peak in planar half-metallic trilayers. *Phys. Rev. B* **2022**, *105*, 104508.

(28) Scammell, H. D.; Li, J. I. A.; Scheurer, M. S. Theory of zero-field superconducting diode effect in twisted trilayer graphene. *2D Materials* **2022**, *9*, 025027.

(29) Yuan, N. F. Q.; Fu, L. Supercurrent diode effect and finite-momentum superconductors. *Proc. Natl. Acad. Sci. U. S. A.* **2022**, *119*, No. e2119548119.

(30) He, J. J.; Tanaka, Y.; Nagaosa, N. A phenomenological theory of superconductor diodes. *New J. Phys.* **2022**, *24*, 053014.

(31) Ilić, S.; Bergeret, F. S. Theory of the Supercurrent Diode Effect in Rashba Superconductors with Arbitrary Disorder. *Phys. Rev. Lett.* **2022**, *128*, 177001.

(32) Zhang, Y.; Gu, Y.; Hu, J.; Jiang, K.General Theory of Josephson Diodes. arXiv:2112.08901 [cond-mat.supr-con], 2021; https://arxiv.org/abs/2112.08901, submission date: 10 Jul 2022 (accessed 2022-08-30).

(33) Qu, F.; van Veen, J.; de Vries, F. K.; Beukman, A. J. A.; Wimmer, M.; Yi, W.; Kiselev, A. A.; Nguyen, B.-M.; Sokolich, M.; Manfra, M. J.; Nichele, F.; Marcus, C. M.; Kouwenhoven, L. P. Quantized Conductance and Large g-Factor Anisotropy in InSb Quantum Point Contacts. *Nano Lett.* **2016**, *16*, 7509−7513.

(34) Chen, Y.; Huang, S.; Pan, D.; Xue, J.; Zhang, L.; Zhao, J.; Xu, H. Q. Strong and tunable spin−orbit interaction in a single crystalline InSb nanosheet. *npj 2D Materials and Applications* **2021**, *5*, 3.

(35) Fuchs, L.; Kochan, D.; Baumgartner, C.; Reinhardt, S.; Gronin, S.; Gardner, G. C.; Lindemann, T.; Manfra, M. J.; Strunk, C.;

Paradiso, N.Anisotropic Vortex Squeezing in Synthetic Rashba Superconductors: A Manifestation of Lifshitz Invariants. arXiv:2201.02512 [cond-mat.supr-con], 2022; https://arxiv.org/abs/2201.02512, submission date: 31 Jan 2022 (accessed 2022-08-30).

(36) Strambini, E.; Iorio, A.; Durante, O.; Citro, R.; Sanz-Fernández, C.; Guarcello, C.; Tokatly, I. V.; Braggio, A.; Rocci, M.; Ligato, N.; Zannier, V.; Sorba, L.; Bergeret, F. S.; Giazotto, F. A Josephson phase battery. *Nat. Nanotechnol.* **2020**, *15*, 656−660.

(37) Moehle, C. M.; Ke, C. T.; Wang, Q.; Thomas, C.; Xiao, D.; Karwal, S.; Lodari, M.; van de Kerkhof, V.; Termaat, R.; Gardner, G. C.; Scappucci, G.; Manfra, M. J.; Goswami, S. InSbAs Two-Dimensional Electron Gases as a Platform for Topological Super-conductivity. *Nano Lett.* **2021**, *21*, 9990−9996.

(38) Chen, Y.; Huang, S.; Mu, J.; Pan, D.; Zhao, J.; Xu, H.-Q. A double quantum dot defined by top gates in a single crystalline InSb nanosheet. *Chinese Physics B* **2021**, *30*, 128501.

(39) Sladek, R. J. Effective Masses of Electrons in Indium Arsenide and Indium Antimonide. *Phys. Rev.* **1957**, *105*, 460−464.

(40) Vurgaftman, I.; Meyer, J. R.; Ram-Mohan, L. R. Band parameters for III−V compound semiconductors and their alloys. *J. Appl. Phys.* **2001**, *89*, 5815−5875.

(41) de la Mata, M.; Leturcq, R.; Plissard, S. R.; Rolland, C.; Magén, C.; Arbiol, J.; Caroff, P. Twin-Induced InSb Nanosails: A Convenient High Mobility Quantum System. *Nano Lett.* **2016**, *16*, 825−833.

(42) Ke, C. T.; Moehle, C. M.; de Vries, F. K.; Thomas, C.; Metti, S.; Guinn, C. R.; Kallaher, R.; Lodari, M.; Scappucci, G.; Wang, T.; Diaz, R. E.; Gardner, G. C.; Manfra, M. J.; Goswami, S. Ballistic superconductivity and tunable π−junctions in InSb quantum wells. *Nat. Commun.* **2019**, *10*, 3764.

(43) de Vries, F. K.; Sol, M. L.; Gazibegovic, S.; op het Veld, R. L. M.; Balk, S. C.; Car, D.; Bakkers, E. P. A. M.; Kouwenhoven, L. P.; Shen, J. Crossed Andreev reflection in InSb flake Josephson junctions. *Phys. Rev. Research* **2019**, *1*, 032031.

(44) Lei, Z.; Lehner, C. A.; Cheah, E.; Mittag, C.; Karalic, M.; Wegscheider, W.; Ensslin, K.; Ihn, T. Gate-defined quantum point contact in an InSb two-dimensional electron gas. *Phys. Rev. Research* **2021**, *3*, 023042.

(45) Litvinenko, K. L.; Nikzad, L.; Pidgeon, C. R.; Allam, J.; Cohen, L. F.; Ashley, T.; Emeny, M.; Zawadzki, W.; Murdin, B. N. Temperature dependence of the electron Landé *g* factor in InSb and GaAs. *Phys. Rev. B* **2008**, *77*, 033204.

(46) Verma, I.; Zannier, V.; Rossi, F.; Ercolani, D.; Beltram, F.; Sorba, L. Morphology control of single-crystal InSb nanostructures by tuning the growth parameters. *Nanotechnology* **2020**, *31*, 384002.

(47) Verma, I.; Salimian, S.; Zannier, V.; Heun, S.; Rossi, F.; Ercolani, D.; Beltram, F.; Sorba, L. High-Mobility Free-Standing InSb Nanoflags Grown on InP Nanowire Stems for Quantum Devices. *ACS Appl. Nano Mater.* **2021**, *4*, 5825−5833.

(48) Salimian, S.; Carrega, M.; Verma, I.; Zannier, V.; Nowak, M. P.; Beltram, F.; Sorba, L.; Heun, S. Gate-controlled supercurrent in ballistic InSb nanoflag Josephson junctions. *Appl. Phys. Lett.* **2021**, *119*, 214004.

(49) Pan, D.; Fan, D. X.; Kang, N.; Zhi, J. H.; Yu, X. Z.; Xu, H. Q.; Zhao, J. H. Free-Standing Two-Dimensional Single-Crystalline InSb Nanosheets. *Nano Lett.* **2016**, *16*, 834−841.

(50) Gazibegovic, S.; Badawy, G.; Buckers, T. L. J.; Leubner, P.; Shen, J.; de Vries, F. K.; Koelling, S.; Kouwenhoven, L. P.; Verheijen, M. A.; Bakkers, E. P. A. M. Bottom-Up Grown 2D InSb Nanostructures. *Adv. Mater.* **2019**, *31*, 1808181.

(51) Zhi, J.; Kang, N.; Li, S.; Fan, D.; Su, F.; Pan, D.; Zhao, S.; Zhao, J.; Xu, H. Supercurrent and Multiple Andreev Reflections in InSb Nanosheet SNS Junctions. *Phys. Status Solidi B* **2019**, *256*, 1800538.

(52) Zhi, J.; Kang, N.; Su, F.; Fan, D.; Li, S.; Pan, D.; Zhao, S. P.; Zhao, J.; Xu, H. Q. Coexistence of induced superconductivity and quantum Hall states in InSb nanosheets. *Phys. Rev. B* **2019**, *99*, 245302.

(53) Rasmussen, A.; Danon, J.; Suominen, H.; Nichele, F.; Kjaergaard, M.; Flensberg, K. Effects of spin-orbit coupling and

spatial symmetries on the Josephson current in SNS junctions. *Phys. Rev. B* **2016**, *93*, 155406.

(54) Dolcini, F.; Houzet, M.; Meyer, J. S. Topological Josephson ϕ_0 junctions. *Phys. Rev. B* **2015**, *92*, 035428.

(55) Davydova, M.; Prembabu, S.; Fu, L. Universal Josephson diode effect. *Science Advances* **2022**, *8*, No. eabo0309.

(56) Hart, S.; Ren, H.; Kosowsky, M.; Ben-Shach, G.; Leubner, P.; Brüne, C.; Buhmann, H.; Molenkamp, L. W.; Halperin, B. I.; Yacoby, A. Controlled finite momentum pairing and spatially varying order parameter in proximitized HgTe quantum wells. *Nat. Phys.* **2017**, *13*, 87−93.

Supporting Information

Josephson Diode Effect in High Mobility InSb Nanoflags

Bianca Turini,[†] Sedighe Salimian,[†] Matteo Carrega,[‡] Andrea Iorio,[†] Elia Strambini,[†] Francesco Giazotto,[†] Valentina Zannier,[†] Lucia Sorba,[†] and Stefan Heun[*,†]

†NEST, Istituto Nanoscienze-CNR and Scuola Normale Superiore, 56127 Pisa, Italy

‡CNR-SPIN, 16146 Genova, Italy

E-mail: stefan.heun@nano.cnr.it

Sample characterization

The InSb nanoflags used in this work and the Nb/Ti–InSb JJs were extensively characterized in previous publications.[1,2] The InSb nanoflags are defect–free zinc–blende structures with high mobility (up to $\mu_e \sim 29500$ cm^{2}V^{-1}s^{-1}) and a large mean free path ($\lambda_e = 500$ nm) at $T = 4.2$ K.[1] We note that the extracted Fermi wavelength ($\lambda_F = 2\pi/k_F = \sqrt{2\pi/n} \sim 30$ nm for carrier concentration $n = 8.5 \times 10^{11}$ cm^{-2}[1]) is of the same order of magnitude as the thickness of the nanoflags ($t \approx 100$ nm):[1,2] by evaluating the number of the active transport modes (≈ 40)[2] and the degeneracy of the vertical subbands, we find that these devices are well placed in the quantum limit with a clear 2D character.

For device fabrication, the nanoflags are placed on a p–doped Si/SiO$_2$ substrate, which acts as a global back–gate. The nanoflags are contacted by 10/150 nm of Ti/Nb, which

defines the superconducting leads, leaving the central region of the nanoflag uncovered. The dimensions of the resulting planar Josephson junctions, length $L = 200$ nm and width $W = 700$ nm, are such that the devices work in the ballistic regime. More details on device fabrication can be found in the supplemental material of Ref. 2. Figure S1a and Figure S1b show the two devices discussed in this manuscript, named G4 and G5, respectively. The two devices, resulting from the same fabrication process, are characterized by the same material and geometric parameters. The superconducting coherence length can be determined as $\xi_s = \hbar v_F / \Delta$,[3–6] where Δ is the gap in the superconductor and v_F the Fermi velocity in the semiconductor. By inserting the value of the Nb gap ($\Delta = 1.28$ meV[2]) and the value of the Fermi velocity of the InSb nanoflags ($v_F = \hbar k_F / m^* = 1.5 \times 10^6$ m/s[2]), we obtain a coherence length much larger than the length of the uncovered region ($\xi_s \approx 750$ nm $> L$). Thus, the devices operate in the short junction regime.

Transport measurements were performed in an Oxford Triton 200 dilution refrigerator with a base temperature of 30 mK. The measurement setup is sketched in Figure S1c. We study the low-temperature magneto-transport of the devices in the presence of an in-plane magnetic field. A relative angle θ ($-180° \leq \theta \leq 180°$) can be set between the orientation of the in-plane magnetic field and the direction of current flow, $\vec{B}_{ip}$ and $\vec{I}$, respectively. The sign of θ is given by the direction of the $\vec{B}_{ip} \times \vec{I}$ vector. With this definition, $\theta = 0°$ for $\vec{B}_{ip} \parallel \vec{I}$ and $\theta = 90°$ for $\vec{B}_{ip} \perp \vec{I}$.

Figure S1d shows a characteristic $V - I$ curve of device G4 measured at $T = 30$ mK and $V_{bg} = 40$ V. We can clearly distinguish the switching (I_{sw}) and the retrapping (I_{rt}) currents.[7] Figure S1e shows that the extent of the superconducting region decreases monotonically with increasing temperature. The data in the 2D plot are collected by performing a sweep from negative to positive bias, so that the upper plane shows the switching current, while the lower one presents the retrapping value. We also measured the opposite sweep direction (from positive to negative bias, see Figure S2). For both sweep directions, we extracted the values of I_{sw} and I_{rt}. They are shown as dots in Figure S1e, overlaid on the 2D plot. The
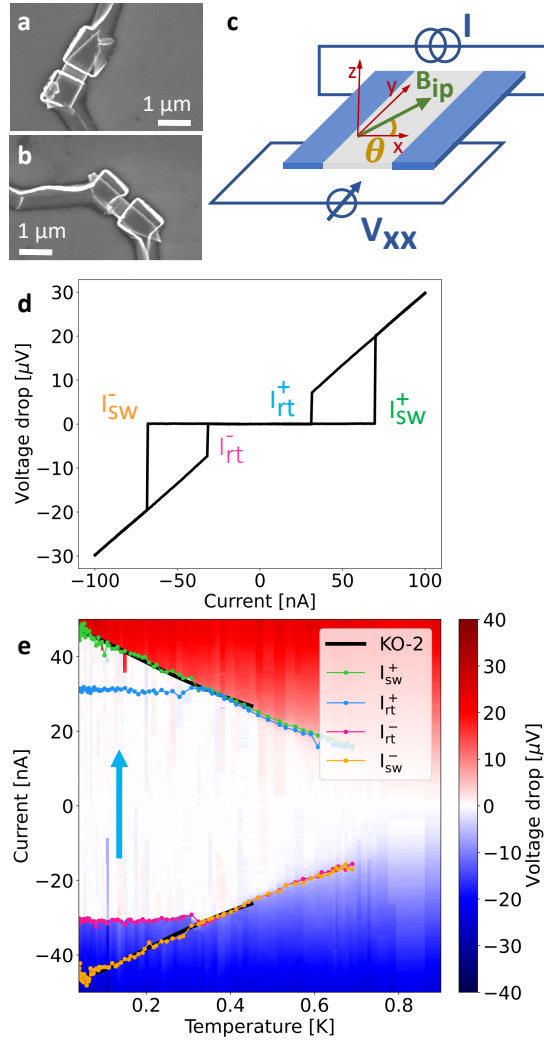
Figure S1: Device characterization. (a,b) SEM images of the two devices, G4 and G5. (c) Sketch of the measurement schematics. Also the angle θ between the orientation of the in-plane magnetic field B_{ip} and the direction of current flow I is indicated. (d) $V - I$ characteristics at $T = 30$ mK. The difference between switching and retrapping current, defined in the plot, is clearly visible. (e) Temperature dependence of the $V - I$ characteristics. The individual spectra were measured sweeping from negative to positive bias values, in the direction indicated by the arrow. Thus, the 2D plot shows the switching trace for positive values of the current and the retrapping trace for the negative ones. The extracted values of $I_{sw}^+, I_{rt}^+, I_{sw}^-, I_{rt}^-$ for each temperature and both sweep directions are shown in green, blue, pink and orange, respectively. The black lines show a fit of the switching currents to the KO-2 model (see text). For (d,e): device G4, $B = 0$ mT, and $V_{bg} = 40$ V.

values of I_{sw} and I_{rt} differ for temperatures lower than ~ 300 mK, consistent with previous measurements.[2] This hysteretic behavior is typical of SNS weak-links[8,9] and is commonly understood as Joule heating of the N region in the dissipative regime.[10–13] In all the following arguments, the switching and retrapping currents are considered separately.

Figure S1e shows the $V - I$ characteristics dependence on temperature for one sweep direction only (from negative to positive current values). For completeness, we report the data acquired in the other direction in Figure S2. In this case, we observe the *retrapping* current values in the positive branch and the *switching* current values for the negative one.
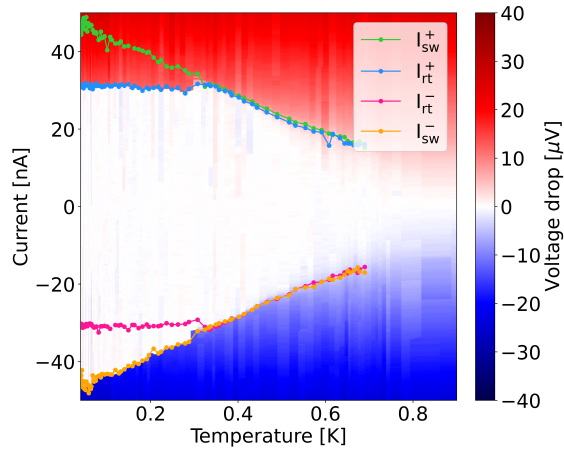

Figure S2: Temperature dependence of the $V-I$ characteristics. The individual spectra were measured sweeping from positive to negative bias. Thus, the 2D plot shows the retrapping trace for positive values of the current and the switching trace for the negative ones. The extracted values of $I_{sw}^+, I_{rt}^+, I_{rt}^-, I_{sw}^-$ for each temperature and both sweep directions are shown in green, blue, pink and orange, respectively. Device G4, $B = 0$ mT, and $V_{bg} = 40$ V.
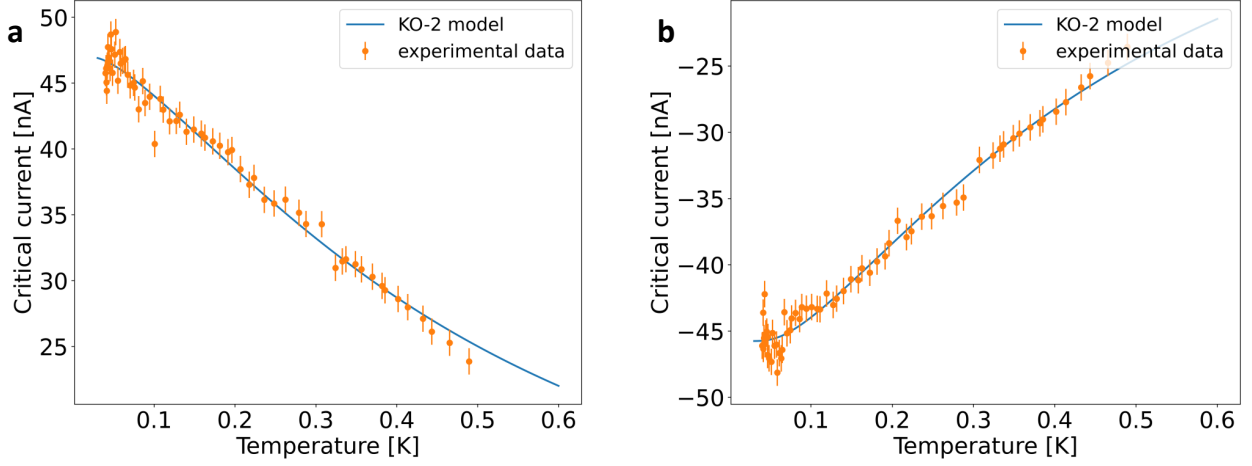
Fitting procedure for the dependence $I_{sw} - T$

Figure S3: Temperature dependence of (a) the positive and (b) the negative switching current. The experimental data are shown as orange dots, together with the measurement error. The blue line is the best fit curve described by the KO-2 model.

The value of the switching current for each temperature is extracted from the 2D maps in Figure S1e and Figure S2. The temperature dependence of the switching current is well described by the Kulik–Omelyanchuk model in the clean limit (KO–2).[14–16] In this case, the current-phase relation at $B = 0$ is described by the following equation:

$$I(\varphi, \tau, T) = I_0 \frac{\sin \varphi}{\sqrt{1 - \tau \sin^2 \varphi/2}} \tanh \left(\frac{\Delta^*}{2k_B T} \sqrt{1 - \tau \sin^2 \varphi/2} \right), \tag{1}$$

where φ is the superconducting phase difference across the junction, τ the transmission coefficient averaged over the transport modes, T the temperature, and I_0 is the critical current for $T = 0$. The induced gap Δ^* is taken as a constant in the range of temperatures under study, thus the temperature range considered for the fit is 0.03 K $< T < 0.5$ K. The value of the positive (negative) critical current is defined as the maximum (minimum) of this function with respect to the phase

$$I_c^+ = \max_{\varphi} I(\varphi, \tau, T) \qquad I_c^- = \min_{\varphi} I(\varphi, \tau, T). \tag{2}$$

The absolute error for the switching current is $\sigma = 1$ nA. The best fit function for the positive and negative branches are reported, together with the experimental data, in Figure S3a and Figure S3b, respectively.

The optimal parameters are consistent for the two data sets. For the positive branch, we obtain:

$$I_0 = (48.1 \pm 0.7) \text{ nA}$$

$$\Delta^* = (111 \pm 3) \quad \mu\text{eV}$$

$$\tau = (0.99 \pm 0.01)$$

Consistent values are obtained for the negative branch:

$$I_0 = (-49 \pm 1) \text{ nA}$$

$$\Delta^* = (104 \pm 4) \quad \mu\text{eV}$$

$$\tau = (0.99 \pm 0.01).$$

The best fits are reported, together with the experimental data, in Figure S3. The good agreement with the KO-2 model indicates that the junctions are working in the ballistic regime, as expected from the value of $\lambda_e > L$. This confirms that the devices are in the ballistic short–junction regime, which leads to a skewed CPR including higher harmonics, crucial for observing the JDE.[17] The extracted value for the induced gap is $\Delta^* = 108 \pm 4 \ \mu\text{eV}$, consistent with the values found in literature.[2] The resulting transmission probability $\tau \sim 0.99$ confirms the high quality of the interfaces in the devices, as previously reported.[2]

Experimental data from device G4

Device G4 shows in average higher values of switching current at low fields, but it is also more noisy. Figure S4a shows the 2D map of voltage drop *versus* in-plane magnetic field (x axis) and current (y axis), for $\theta = -152°$. The skewness of the pattern is reversed with respect to what shown in Figure 1 of the main text, consistently with the difference of angle between the two devices (see main text). In this case, the asymmetry in the retrapping current is not visible with our experimental resolution.
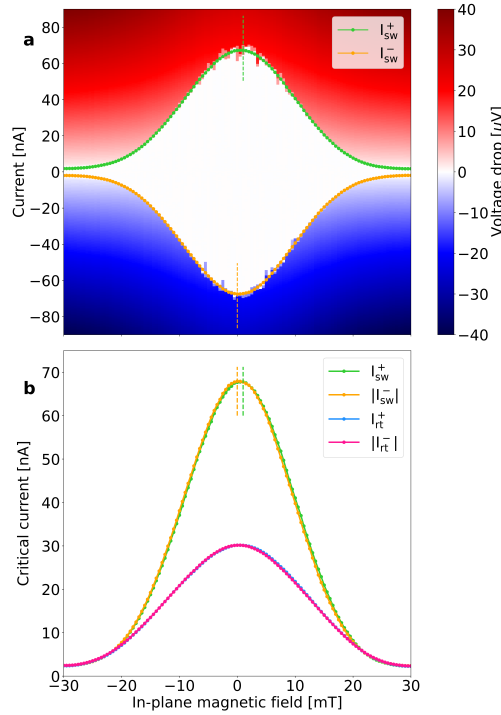

Figure S4: Switching current dependence on in-plane magnetic field. (a) Voltage drop across the junction versus in-plane magnetic field. The superconducting phase, defined by dissipation–less charge transport, corresponds to the white region. The green (orange) dots indicate the positive (negative) switching current, as defined in the main text. (b) The switching current shows a clear asymmetry between the positive and negative branches, shown in green and orange, respectively. The negative branch is higher for positive values of the magnetic field, and the relation is reversed for negative field. The blue and pink lines correspond to the positive and negative retrapping current. Device G4, $T = 30$ mK, and $V_{bg} = 40$ V.
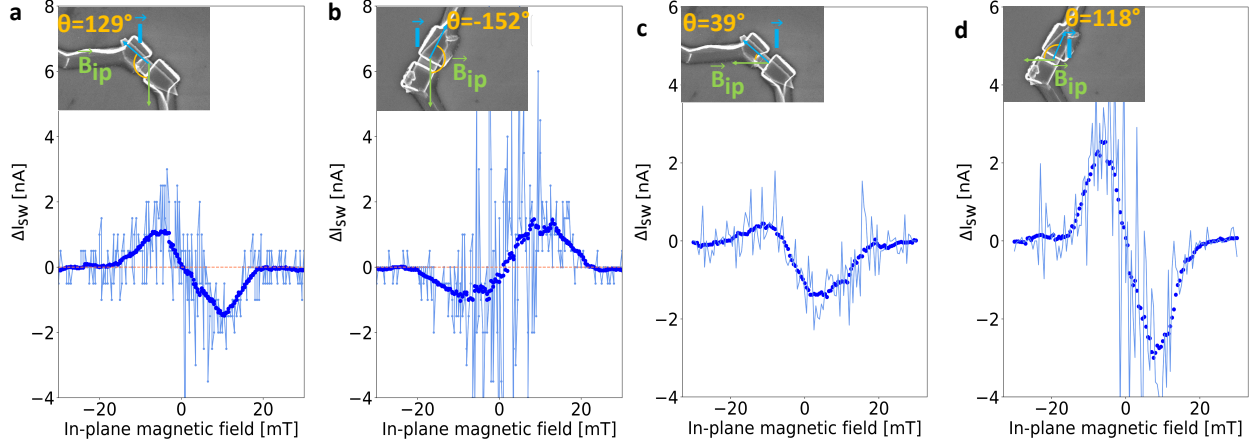
Raw data for ΔI_{sw}

Figure S5: Asymmetry in the switching current with respect to the in–plane magnetic field, for four different relative orientations between the current flow and the magnetic field direction, as indicated in the insets. (a) Asymmetry for Device G5, which is placed at an angle of $\theta = 129°$ with respect to the field direction. (b) Device G4, $\theta = -152°$. (c) Device G5, $\theta = 39°$. (d) Device G4, $\theta = 118°$. For all measurements, $T = 30$ mK and $V_{bg} = 40$ V.

In Figure S5 we show raw data for all the measured orientations, together with the curves resulting from the smoothing procedure, as explained in the following.

The InSb nanoflags under study exhibit stochastic switching, i.e. the value of the switching current is a stochastic quantity, especially at low temperature. For this reason, the dependence of the switching current is masked with noise. This phenomenon is due to quantum fluctuations and of great interest in the study of phase dynamics.[18]

To distinguish the general trend from fluctuations, we have performed a smoothing procedure of the data with the Savitzky-Golay (SG) filter.[19] The SG algorithm is defined by two parameters: the width (W) of the window of data to be considered in the analysis and the order (n) of the polynomial expression used in the least-square fit. In Figure 2 of the main text and in Figure S4, the chosen parameters are $W = 31$, $n = 2$.

In Figure S5a,b, the data from the first acquisition set are reported. The angle θ (see main text) was set to $\theta = -152°$ for G4 and $\theta = 129°$ for G5. The light blue lines stand for the raw data, while the blue dots represent the result of the smoothing procedure. Here, we

have used $W = 31$, $n = 1$ for smoothing.

In Figure S5c,d, the angle θ was set to $\theta = 118°$ for G4 and $\theta = 39°$ for G5. In this case, 17 curves were acquired for each value of magnetic field, resulting in 17 values of asymmetry, which are averaged before performing the smoothing procedure. The averaged values are represented by the light blue line, while the smoothed data are shown as blue dots. The smoothing parameters are $W = 15$, $n = 1$.

JDE in the retrapping current

The switching and the retrapping current are clearly distinguishable in these systems, up to $T \sim 300$ mK. We have observed the JDE also in the retrapping data, even if weaker. Considering that the difference between the two is related to the higher effective temperature of the electron gas in the retrapping branch, we can use the same arguments as in Section (the temperature dependence of the JDE) to explain this reduction.
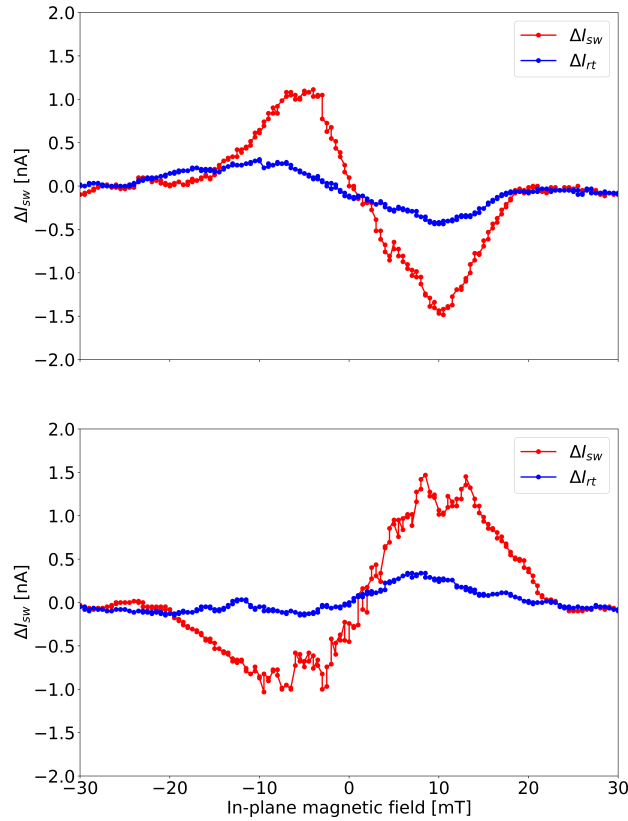

Figure S6: Asymmetry in the switching and retrapping current with respect to the in–plane magnetic field, represented by the red and blue dots, respectively. The effect is strongly reduced in the latter, while the polarity and the shape of the curves are maintained.

Parallel component of the in-plane magnetic field

To disentangle the contributions of the parallel $(B_{ip,\parallel})$ and perpendicular $(B_{ip,\perp})$ components of the in-plane magnetic field, computed with respect to the direction of current flow, we mapped the measured data on the effective $B_{ip,\parallel} = B_{ip}\cos(\theta)$. In this case, there is a clear mismatch in the shape of the asymmetry for different angles. More importantly, while the polarity in the $B_{ip,\perp}$ dependence is the same for each θ (see Figure 2c of the main text), this is not observed in ΔI_{sw} vs. $B_{ip,\parallel}$. This evidence is consistent with the interpretation of a dominant Rashba-type SOI (see main text).
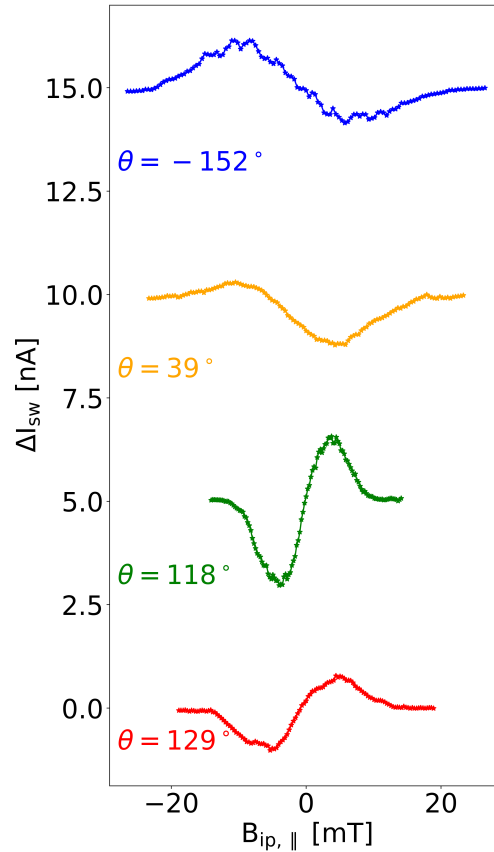

Figure S7: Behavior of JDE with parallel component of the in-plane magnetic field. Asymmetry versus the component of the magnetic field parallel to the current flow. No clear trend of visible. The curves are shifted by 5 nA each for clarity.

Back-gate dependence of the JDE

As previously shown,[2] these devices act as Jo-FETs, i.e., the switching current is tunable with gate voltage (V_{bg}). In Figure S8a, measured at $B = 0$, the 2D map shows how the extent of the supercurrent changes with V_{bg}. Data in Figure S8b–d are sampled in presence of a magnetic field of $B_{ip} = -6$ mT, $B_{ip} = -8$ mT, and $B_{ip} = -10$ mT, respectively. The resulting asymmetry is shown in Figure 2d of the main text. Despite the strong variation that the field effect induces on I_{sw}, which is over 50 nA in the range considered, there is no visible effect on ΔI_{sw} (see main text).
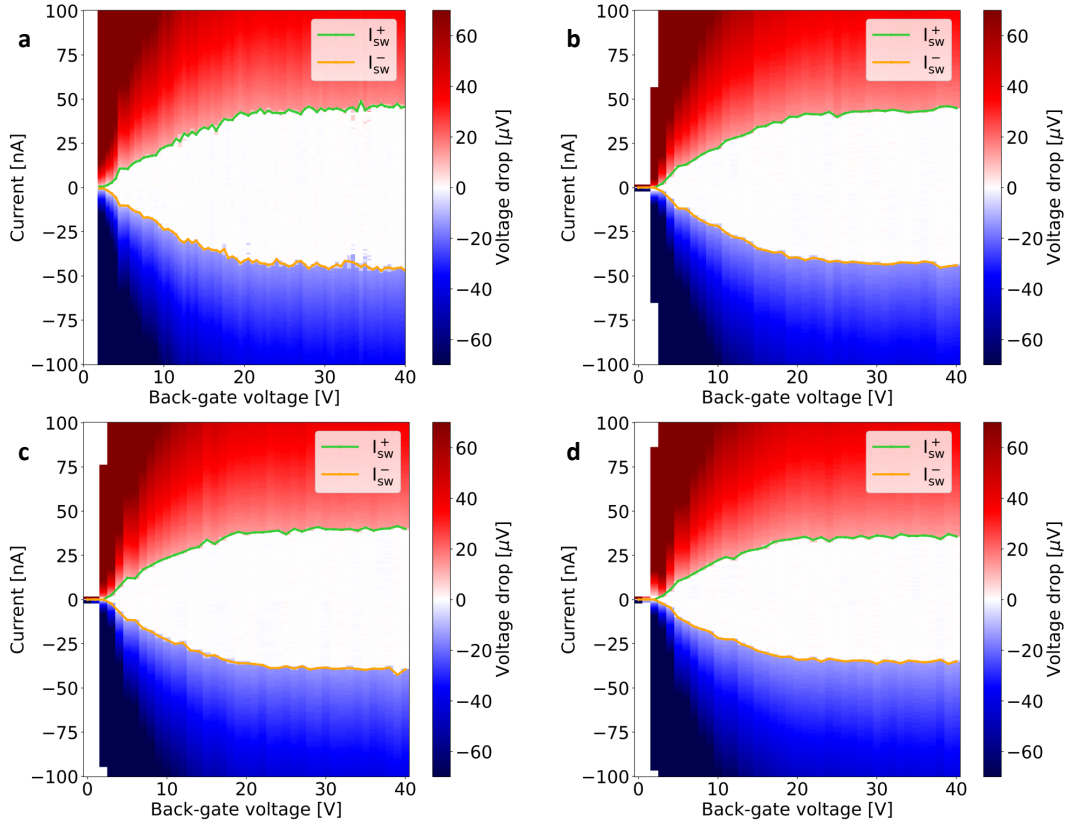

Figure S8: Electrostatic control of the switching current. The color map represents the voltage drop as a function of back gate voltage and current. The in–plane magnetic field was fixed to different values for each acquisition: (a) $B_{ip} = 0$, (b) $B_{ip} = -6$ mT, (c) $B_{ip} = -8$ mT, and (d) $B_{ip} = -10$ mT. The positive (negative) switching current I_{sw}^+ (I_{sw}^-) is shown with green (orange) dots. Device G5, $T = 30$ mK.

Temperature dependence of the JDE

As explained in the main text, the JDE is strongly reduced with increasing temperature. Figure S9 shows the interference patterns for $T = 30$ mK, $T = 100$ mK, $T = 150$ mK, and $T = 200$ mK. The last acquisition was not completed since the data already demonstrated that the effect had faded completely. It is clear from the 2D maps that the value of the switching current is very little reduced for such small changes of temperature, consistent with Figure S1e.
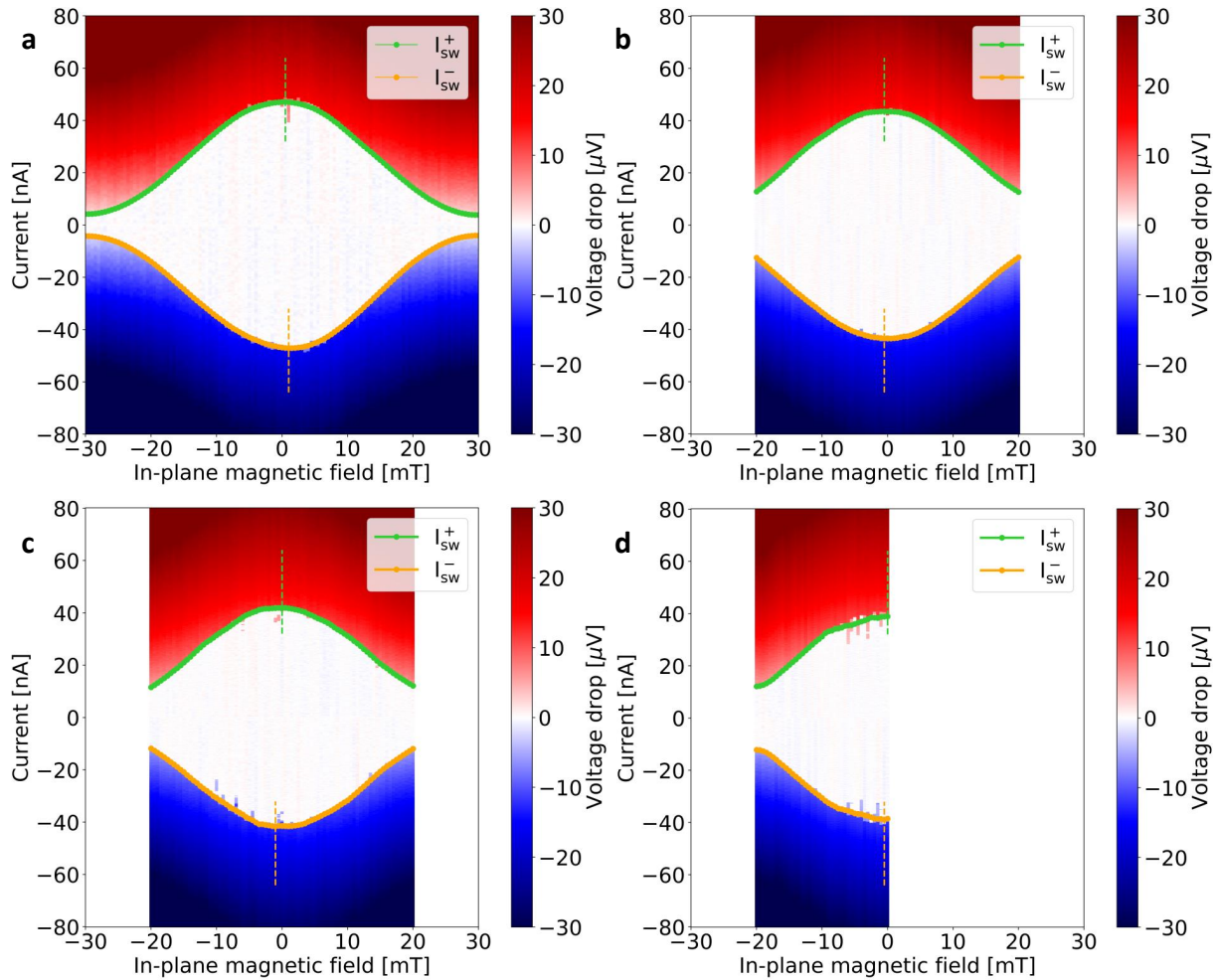

Figure S9: Interference patterns measured at different temperatures. The temperature was fixed to 30, 100, 150, 200 mK for the data in a,b,c,d, respectively. The positive (negative) switching current I_{sw}^+ (I_{sw}^-) is shown with green (orange) dots.

Universal maximum in ΔI_{sw}

We find the maximum of the asymmetry ΔI_{sw} with respect to $B_{ip,\perp}$, by making use of the expression

$$\Delta I_c = \text{sgn}(q)\left(\frac{4e|q|v_F}{\pi\hbar} - \frac{e\Delta^*}{\hbar}\left[1 - \sqrt{1 - \left(\frac{qv_F}{\Delta^*}\right)^2}\right]\right) \tag{3}$$

as reported in.[20] The maximum is reached for

$$q_0 v_F = \sqrt{\frac{16}{\pi^2 + 16}}\ \Delta^* \approx 0.78\,\Delta^*. \tag{4}$$

To compute the value of $B_{max} = 58$ mT, we use $\Delta^* = 108\ \mu$eV, $g_{ip}^* = 25$.[21,22]

References

(1) Verma, I.; Salimian, S.; Zannier, V.; Heun, S.; Rossi, F.; Ercolani, D.; Beltram, F.; Sorba, L. High-Mobility Free-Standing InSb Nanoflags Grown on InP Nanowire Stems for Quantum Devices. *ACS Appl. Nano Mater.* **2021**, *4*, 5825–5833.

(2) Salimian, S.; Carrega, M.; Verma, I.; Zannier, V.; Nowak, M. P.; Beltram, F.; Sorba, L.; Heun, S. Gate-controlled supercurrent in ballistic InSb nanoflag Josephson junctions. *Appl. Phys. Lett.* **2021**, *119*, 214004.

(3) Lee, G.-H.; Lee, H.-J. Proximity coupling in superconductor-graphene heterostructures. *Rep. Prog. Phys.* **2018**, *81*, 056502.

(4) de Vries, F. K.; Sol, M. L.; Gazibegovic, S.; op het Veld, R. L. M.; Balk, S. C.; Car, D.; Bakkers, E. P. A. M.; Kouwenhoven, L. P.; Shen, J. Crossed Andreev reflection in InSb flake Josephson junctions. *Phys. Rev. Research* **2019**, *1*, 032031.

(5) Zhi, J.; Kang, N.; Li, S.; Fan, D.; Su, F.; Pan, D.; Zhao, S.; Zhao, J.; Xu, H. Supercur-

rent and Multiple Andreev Reflections in InSb Nanosheet SNS Junctions. *Phys. Status Solidi B* **2019**, *256*, 1800538.

(6) Banszerus, L.; Libisch, F.; Ceruti, A.; Blien, S.; Watanabe, K.; Taniguchi, T.; Hüttel, A. K.; Beschoten, B.; Hassler, F.; Stampfer, C. Minigap and Andreev bound states in ballistic graphene. arXiv:2011.11471 [cond-mat.mes-hall], 2021.

(7) We note that the data of Ref. 2, for which this hysteretic behavior was not observed, were obtained at $T = 250$ mK, i.e., at a higher temperature than employed here.

(8) Tinkham, M. *Introduction to superconductivity*; McGraw-Hill, 1996.

(9) Guiducci, S.; Carrega, M.; Biasiol, G.; Sorba, L.; Beltram, F.; Heun, S. Toward Quantum Hall Effect in a Josephson Junction. *Phys. Status Solidi RRL* **2019**, *13*, 1800222.

(10) Schäpers, T. *Superconductor / semiconductor junctions*; Springer, 2001.

(11) Courtois, H.; Meschke, M.; Peltonen, J. T.; Pekola, J. P. Origin of Hysteresis in a Proximity Josephson Junction. *Phys. Rev. Lett.* **2008**, *101*, 067002.

(12) Fornieri, A. Josephson effect in ballistic semiconductor nanostructures. M.Sc. thesis, University of Pisa, 2013.

(13) Guiducci, S.; Carrega, M.; Taddei, F.; Biasiol, G.; Courtois, H.; Beltram, F.; Heun, S. Full electrostatic control of quantum interference in an extended trenched Josephson junction. *Phys. Rev. B* **2019**, *99*, 235419.

(14) Kulik, I. O.; Omel'yanchuk, A. N. Properties of superconducting microbridges in the pure limit. *Sov. J. Low Temp. Phys.* **1977**, *3*, 459–462.

(15) Golubov, A. A.; Kupriyanov, M. Y.; Il'ichev, E. The current-phase relation in Josephson junctions. *Rev. Mod. Phys.* **2004**, *76*, 411–469.

(16) Lee, G.-H.; Kim, S.; Jhi, S.-H.; Lee, H.-J. Ultimately short ballistic vertical graphene Josephson junctions. *Nature Communications* **2015**, *6*, 6181.

(17) Baumgartner, C.; Fuchs, L.; Costa, A.; Reinhardt, S.; Gronin, S.; Gardner, G. C.; Lindemann, T.; Manfra, M. J.; Faria Junior, P. E.; Kochan, D.; Fabian, J.; Paradiso, N.; Strunk, C. Supercurrent rectification and magnetochiral effects in symmetric Josephson junctions. *Nature Nanotechnology* **2022**, *17*, 39–44.

(18) Haxell, D. Z.; Cheah, E.; Křížek, F.; Schott, R.; Ritter, M. F.; Hinderling, M.; Belzig, W.; Bruder, C.; Wegscheider, W.; Riel, H.; Nichele, F. Large Quantum Fluctuations in Planar Josephson Junctions. arXiv:2204.05619 [cond-mat.mes-hall], 2022.

(19) Savitzky, A.; Golay, M. J. E. Smoothing and Differentiation of Data by Simplified Least Squares Procedures. *Analytical Chemistry* **1964**, *36*, 1627–1639.

(20) Davydova, M.; Prembabu, S.; Fu, L. Universal Josephson diode effect. *Science Advances* **2022**, *8*, eabo0309.

(21) Qu, F.; van Veen, J.; de Vries, F. K.; Beukman, A. J. A.; Wimmer, M.; Yi, W.; Kiselev, A. A.; Nguyen, B.-M.; Sokolich, M.; Manfra, M. J.; Nichele, F.; Marcus, C. M.; Kouwenhoven, L. P. Quantized Conductance and Large g-Factor Anisotropy in InSb Quantum Point Contacts. *Nano Lett.* **2016**, *16*, 7509–7513.

(22) de la Mata, M.; Leturcq, R.; Plissard, S. R.; Rolland, C.; Magén, C.; Arbiol, J.; Caroff, P. Twin-Induced InSb Nanosails: A Convenient High Mobility Quantum System. *Nano Lett.* **2016**, *16*, 825–833.